Research Article Vol. 31, No. 2 / 16 Jan 2023 / Optics Express 2102
Optics EXPRESS

Design of a dynamic multi-topological charge graphene orbital angular momentum metalens

GUIYUAN CAO,[1] HAN LIN,[2] BAOHUA JIA,[2,3] XIAOCONG YUAN,[1] MICHAEL SOMEKH,[1,4] AND SHIBIAO WEI[1,*]

[1]*Nanophotonics Research Center, Shenzhen Key Laboratory of Micro-Scale Optical Information Technology, Shenzhen University, Shenzhen 518060, China*
[2]*School of Science, RMIT University, Melbourne, VIC 3000, Australia*
[3]*The Australian Research Council (ARC) Industrial Transformation Training Centre in Surface Engineering for Advanced Materials (SEAM), RMIT University, Melbourne, VIC 3000, Australia*
[4]*Faculty of Engineering, University of Nottingham, Nottingham NG7 2RD, UK*
[*]*weishibiao@szu.edu.cn*

Abstract: Traditional OAM generation devices are bulky and can generally only create OAM with one specific topological charge. Although metasurface-based devices have overcome the volume limitations, no tunable metasurface-based OAM generators have been demonstrated to date. Here, a dynamically tunable multi-topological charge OAM generator based on an ultrathin integrable graphene metalens is demonstrated by simulation using the detour phase technique and spatial multiplexing. Different topological charges can be designed on different focal planes. Stretching the OAM graphene metalens allows the focal plane and the topological values to be changed dynamically. This design method paves an innovative route toward miniaturization and integrating OAM beam-type photonic devices for practical applications.

1. Introduction

Optical beams that carry orbital angular momentum (OAM), which feature doughnut-shaped intensity distributions, have become a hot research topic since they were discovered by Allen et al. in 1992 [1]. It is well known that optical beams that carry OAM have helical phase fronts with an azimuthal phase term of $\exp(il\theta)$, where θ is the azimuthal angle and l is the topological charge. This topological charge l can have any value between $-\infty$ and $+\infty$, and its sign determines the handedness of the OAM beam. Importantly, OAM beams that carry different integer topological charges are inherently orthogonal to each other, providing a new degree of freedom for information encoding. The special characteristics of OAM beams have enabled and boosted developments in many research areas and technologies, including optical data storage [2], optical communications [3], quantum information processing [4,5], global weather pattern research [6], super-resolution imaging [7], trapping [8], and optical tweezers [9,10].

Continuing development of OAM-based technologies such as optical communications and optical tweezers means an urgent need for a dynamic tuning technique for OAM, which will require a dynamic OAM generator. Currently, most OAM generators are static, including Q-plates [11], cylindrical lens mode converters [12,13], fiber mode couplers [14], spiral phase plates [15,16], fork gratings [17], bound states in the continuum (BIC) based photonic crystal [18], and parts of metasurface OAM generators [19,20]. These methods and devices have all demonstrated the successful generation of OAM-carrying beams and even multi-OAM-carrying beams. However, once these devices have been fabricated, their OAM is fixed, which greatly limits their use in devices and systems that require a dynamic tuning capability. OAM generators based on spatial light modulators [21,22] are one possible solution, but their bulk limits their use amid the trend for integrated and miniaturized optics. Recently, researchers have developed OAM generators that can tune the OAM topological charges or OAM modes dynamically using

#480946 https://doi.org/10.1364/OE.480946
Journal © 2023 Received 16 Nov 2022; revised 23 Dec 2022; accepted 23 Dec 2022; published 6 Jan 2023

Optics EXPRESS

BIC-based photonic crystal and metasurfaces [23–26]. However, these devices are limited by their design and fabrication technologies. Their tuning ability is confined to the two orthogonal polarizations, or their tuning wavelengths are in the microwave band. Additionally, there has been no demonstration of tunable metasurface OAM generators for operation in the communication and visible bands. Therefore, dynamically tunable, integratable, and multi-topological charge OAM generation devices that can be fabricated with low-cost and simple processes are highly desired to enable the miniaturization and integration of optical instruments.

Recently, ultrathin diffractive devices based on graphene and graphene derivatives [27,28] have been attracting extensive research attention. The mechanical robustness, outstanding thermal stability, and chemical and biological stability of the graphene family of materials allow for the broad application of these materials, not only in daily life but also in extreme environments [29]. In addition, ultrathin graphene-based devices can be fabricated using low-cost and scalable one-step laser writing techniques [30,31], and both phase and amplitude manipulation [32,33] of their wavefronts can be realized simultaneously. These properties make these graphene and graphene derivative-based devices stand out from devices composed of other two-dimensional materials that have been developed to support miniaturization and integration of photonic devices. Recently, we demonstrated a varifocal graphene metalens [27] that was designed using the detour phase technique; the graphene metalens was fabricated on a stretchable substrate, a focal length tuning range of more than 20% was achieved, and zoom imaging of different objects using this metalens was demonstrated. In this paper, we propose and provide a numerical demonstration of a tunable graphene OAM metalens with multiple focal planes that combines graphene metalenses and spiral phase plates into a single design. Although this method can be applied to other two-dimensional materials, the graphene and graphene family materials are chosen to simulate the tunable OAM metalens because of their excellent properties and can be stably stuck to PDMS to realize stretchable devices [27]. Different OAM topological charges

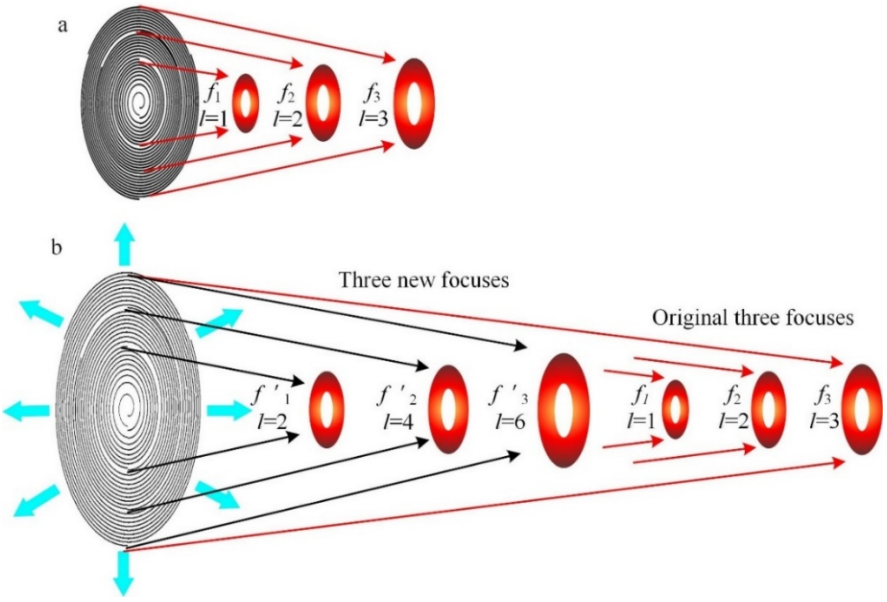

Fig. 1. (a) Graphene OAM metalens with three focal planes that correspond to three different topological charges. (b) Transversely stretching of the graphene OAM metalens enhances the second-order diffraction, leading to the emergence of new focal planes with different topological charges.

Optics EXPRESS

can be generated in different focal planes using the graphene OAM metalens, as illustrated in Fig. 1(a). Furthermore, as shown in Fig. 1(b), transverse stretching of the metalens causes new focal planes with different topological charges to emerge because of the resulting enhancement of the second-order diffraction, which gives this graphene OAM metalens the ability to modulate the OAM topological charges dynamically. The proposed ultrathin graphene OAM metalens will likely find a wide range of applications, including miniaturized or highly compact optical manipulation and communications devices.

2. Design method and simulation results

Figure 2(a) shows the design method for the multifocal graphene OAM metalens. The method comprises three steps, and the first step is to design the graphene metalens. The graphene metalens consists of concentric reduced graphene oxide (rGO) rings, which can be fabricated using the direct laser writing method to reduce graphene oxide film. The radius of each rGO ring can be designed by both the detour phase [34] and Fresnel methods [35], as the Fresnel method offers a higher focusing efficiency, we use it to design the converging phase component of graphene metalens in this paper. The radius of each rGO ring can be expressed as $r_n = \sqrt{n\lambda f + n^2\lambda^2/4}$, where n is a positive integer, λ is the incident beam wavelength, and f is the designed focal length of the graphene metalens. Here, we design three graphene metalenses with different focal lengths. The three focal lengths were designed to be $f_1 = 100\,\mu m$, $f_2 = 200\,\mu m$, and $f_3 = 300\,\mu m$ to reduce the mutual interference among their focal spots. The second step involves OAM phase loading on the graphene metalens. To generate an OAM with a topological charge l, the wavefront phase distribution should satisfy the relation $\phi(x, y) = l \times \mathrm{atan}(y/x)$, where the Cartesian coordinates are represented by (x, y). We use the detour phase technique to apply the phase to the graphene metalens. The detour phase technique was introduced by Brown and Lohmann in 1966 [36] and has been used widely in holography, optical signal processing, and lens design applications [34,37,38]. When using the detour phase technique, wavefront modification can be realized through slight variations in the locations of the rGO rings. Therefore, to realize a phase distribution of $\phi(x, y)$, the location shift of each rGO ring can be expressed using $\Delta d = \phi(x, y) \times \frac{\lambda}{2\pi \sin(atan\left(\sqrt{x^2+y^2}/f\right)}$. OAM with arbitrary topological charge numbers can also be added to the graphene metalens; here, we select $l = 1$, 2, and 3, corresponding to f_1, f_2, and f_3, respectively, as examples. The third step involves the spatial combination of these OAM graphene metalenses. The graphene metalens with the shortest focal length was set in the inner zone, and the metalenses with longer focal lengths were set in the outer zones. There are three boundaries, designated r_1, r_2, and r_3, in the combined graphene OAM metalens, as shown in Fig. 2(a). The areas of these three zones should also be equal to obtain three foci with equal intensities. Therefore, the relationship $r_1 : r_2 : r_3 = \sqrt{1} : \sqrt{2} : \sqrt{3}$ should be satisfied. Furthermore, when the density of the rGO rings in the different zones was considered, a slight optimization was applied. Therefore, under the condition that the width of the rGO rings was 0.4 μm, three zones with $r_1 = 128\,\mu m$, $r_2 = 168\,\mu m$, and $r_3 = 200\,\mu m$ were applied to the three-focus graphene OAM metalens. It is also important to note that OAM metalenses with additional foci can be designed readily based on the combination method used here. In real applications, the Gaussian beams are usually used as the incident beam. Fractional OAM states will be created if there is off-axis illumination [39,40]. Therefore, an enlarged Gaussian beam should be used to avoid this situation. In this simulation, as the graphene OAM metalens is on micrometer-scale, the centimeter scale Gaussian beam can be approximated a plane wave considering the small size of our graphene OAM metalens. The wavelength of this plane wave is 633 nm. The thickness of the graphene OAM metalens is 200 nm. Figure 2(b) shows the intensity distribution on the y-z plane, which was calculated based on the Rayleigh-Sommerfeld diffraction theory [41]. Three focused doughnut patterns with nearly equal intensities are shown clearly and discretely. The accuracy of the focal

Optics EXPRESS

plane locations at 100 µm, 200 µm, and 300 µm, as we designed, verifies the design accuracy of the proposed method. The intensity and phase distributions in the *x*-*y* plane (indicated by the white dashed lines) are shown in Figs. 2(c1) and c2, 2(d1) and d2, and 2(e1) and e2, respectively. The phase distributions in these three *x*-*y* planes verify the clear topological charge numbers of $l = 1$, $l = 2$, and $l = 3$, as designed. The radii of the three focused doughnut shapes increase with the increase in the topological charges as expected. Therefore, a three-focus graphene OAM metalens is designed theoretically.

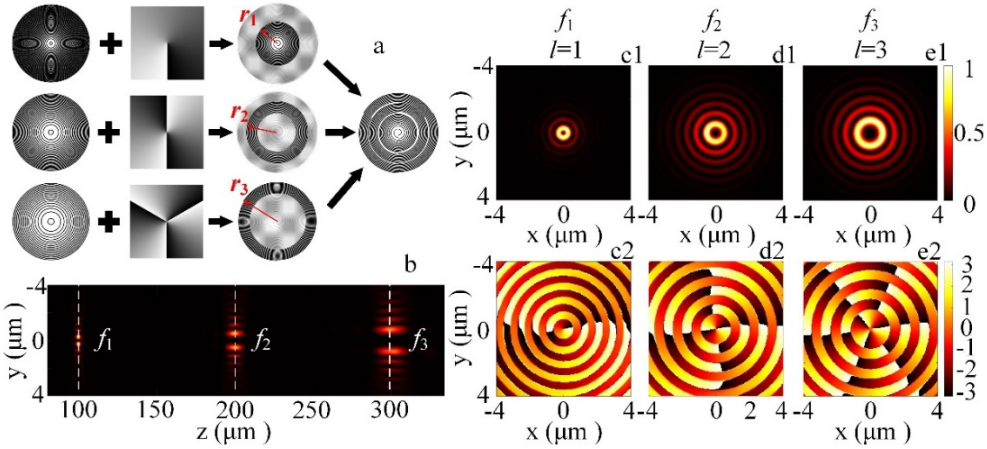

Fig. 2. (a) Design schematic of graphene OAM metalens with three focal planes produced by spatial multiplexing. (b) Normalized intensity distributions of the three doughnut shaped foci in the y-z plane. (c1), (c2) Normalized intensity and phase distributions, respectively, of the focus at f_1 with topological charge $l = 1$. (d1), (d2) Normalized intensity and phase distributions, respectively, of the focus at f2 with topological charge $l = 2$. (e1), (e2) Normalized intensity and phase distributions, respectively, of the focus at f3 with topological charge $l = 3$.

Dynamic tuning of the focal length and the OAM topological charge number is challenging and remains a hot research topic in the miniaturization and integration of OAM generation devices. Lateral stretching is one possible solution that does not require longitudinal movement, thus allowing the thickness of the entire device to be minimized. Our previous work [27] demonstrated a varifocal graphene metalens that used a stretching mechanism. Here, we use a similar methodology to study and summarize the focal length changes using the stretch ratio (SR) of the three-focus graphene metalens without the OAM phase being loaded. The focal length is expected to increase parabolically with increasing SR, as shown in Fig. 3(a). Generally, our design is based on the first diffraction order, meaning the first diffraction order constitutes the main focal spot. There are also higher-order diffractions but with a negligible contribution to focal spots. The first diffraction order is the strongest when the SR is small (i.e., < 1.2). But as the SR increases further, the ring spacing is also enlarged, which strengthens the higher diffraction order and results in new focal spots. As a result, it is possible to tune the topological charges of this generated OAM. When SR > 1.3, the second diffraction order becomes non-negligible, which contributes to a new focal spot. The latter simulation results show a two-fold increase of the topological charge, which confirms to our assertion that dynamic tuning of the OAM topological charge through a stretching mechanism. In addition, as the SR increase, the relative power of the second order becomes larger than the first diffraction order. As shown in Fig. 3(a) and (c), a clear focus at f'_3 appears when SR = 1.3, and then the foci f'_2 and f'_1 emerge when SR = 1.4 and 1.6, respectively. These new foci represent the second-order diffraction of the OAM

Optics EXPRESS

graphene metalens with the double-phase modulation profile of the OAMs. Figure 3(b) shows the designed structures for the three-focus graphene OAM metalens in the cases where the SR is 1.1, 1.5, and 2. The corresponding normalized intensity distributions are shown in Fig. 3(c). Only three doughnut-shaped foci within the focal region occur when SR = 1.1 (first row, Fig. 3(c)). In comparison, when SR = 1.5, higher-order doughnut-shaped foci appear at f'_3 and f'_2 in the new focal regions. In this particular design, the focus of the first order at f_1 overlaps slightly with the second order focus at f'_3 (second row, Fig. 3(c)). Then, by stretching the metalens further to SR = 2, the focus at f'_1 appears (third row, Fig. 3(c)). It is also worth mentioning that, because of the different sizes of the focused doughnut profiles, the covered or hidden doughnut f_1 appears in the three-focus OAM graphene metalens, as shown in Fig. 3(c), when SR = 1.5 and 2.

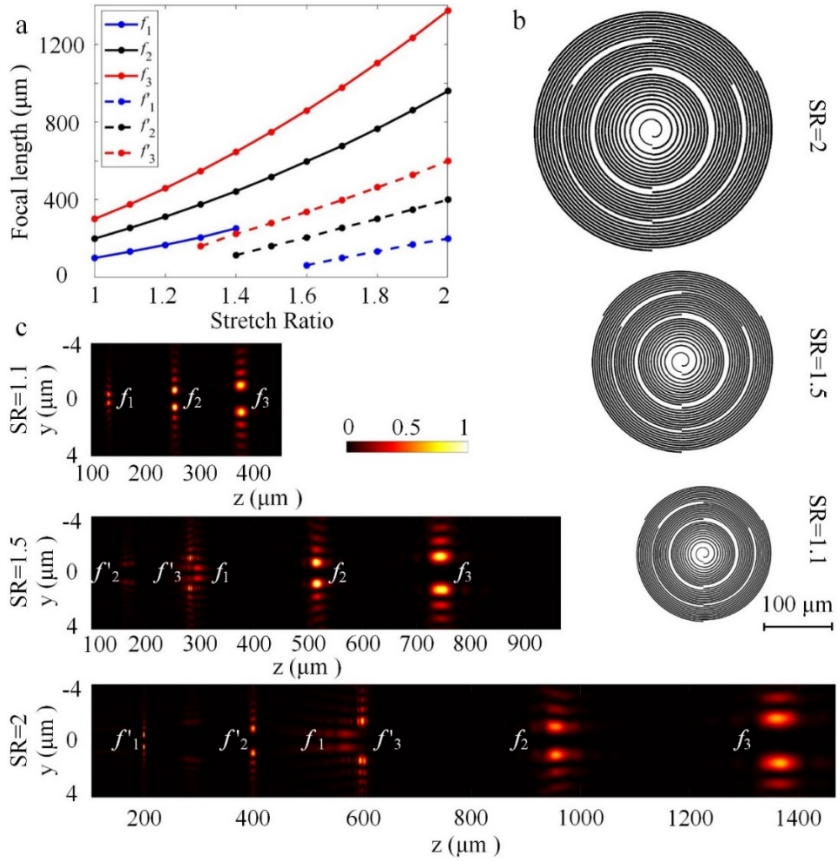

Fig. 3. (a) Focal length change plot versus different SR values for the three-focus graphene metalens. (b) Structures of the three-focus graphene OAM metalens when SR = 1.1, 1.5, and 2. (c) Normalized intensity distributions in the y-z planes for the three-focus graphene OAM metalens when SR = 1.1, 1.5, and 2.

The intensity and phase distributions in the *x*-*y* planes of these doughnut-shaped foci at f_1, f_2, and f_3 for SR = 1.1, 1.5, and 2 are shown in Fig. 4. The figure shows that the radii of the doughnut-shaped foci occurring at f_2 and f_3 (Figs. 4(b) and (c) increase with increasing SR because of the reduction in the effective numerical aperture (NA) of the metalens. In addition, the topological charges remain unchanged, as shown in the phase distributions. However, a different phenomenon can be observed in the doughnut-shaped focus at f_1 (Fig. 4(a)). When SR = 1.5, the topological charge of $l = 1$ can be found at the center of the focal region. However, a topological

Optics EXPRESS

charge of $l = 6$ can be found surrounding the central area that is caused by the interference from the higher diffraction order, which corresponds to the newly generated focus at f'_3, as explained above. By changing the interference condition via further stretching of the lens to SR = 2, the topological charge is then restored to $l = 1$ because of the separation of the foci at f_1 and f'_3.

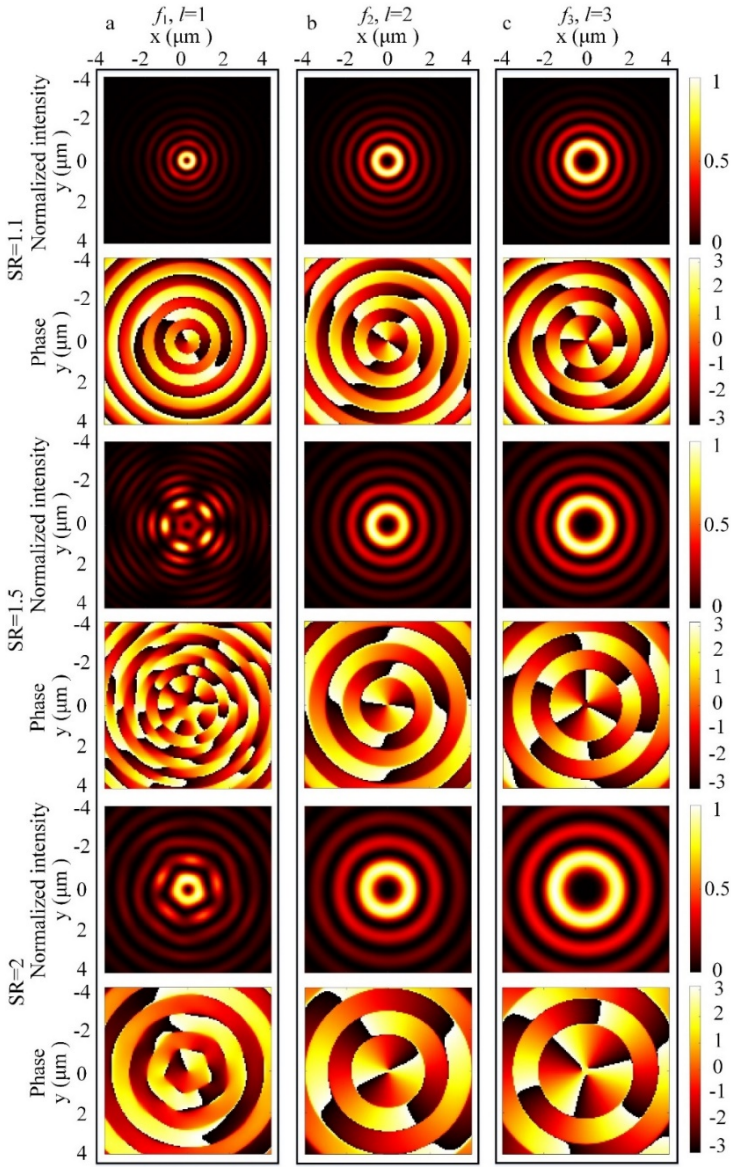

Fig. 4. Normalized intensity and phase distributions on the x-y planes of the focused doughnut shapes. (a) The focused doughnut shapes and phase distributions on the x-y plane of f_1 when SR is 1.1, 1.5 and 2, respectively. (b) The focused doughnut shapes and phase distributions on the x-y plane of f2 when SR is 1.1, 1.5 and 2, respectively. (c) The focused doughnut shapes and phase distributions on the x-y plane of f3 when SR is 1.1, 1.5 and 2, respectively. The topological charges remain at 1, 2, and 3, respectively.

To show the topological charges of the new foci, we perform further simulations of the intensity and phase distributions on the *x*-*y* planes of f'_1, f'_2, and f'_3, as shown in Fig. 5. The results

Optics EXPRESS

show that the topological charges of the three second-order foci at f'_1, f'_2, and f'_3 are $l = 2$, 4, and 6, respectively, which are twice the values of the corresponding topological charges at f_1, f_2, and f_3, respectively. Given that the structure of the graphene metalens is a type of grating structure, we consider the grating equation $\Delta r \sin\theta_m = m\lambda$, where Δr is the ring space between two adjacent rings, θ_m is decided by the corresponding radius of ring and focal length ($\tan\theta_m = r/f$), and m is the diffraction order. For the original graphene metalens, $m = 1, f_1, f_2$, and f_3 are the corresponding first-order diffraction. And when a spiral phase distribution of $\phi(x,y)$ is added into the graphene metalens, the location shift of each ring is $\Delta d = \phi(x,y)\lambda/(2\pi\sin\theta_1)$. When $m = 2$, namely the second-order diffraction, the relationship $\sin\theta_2 = 2\sin\theta_1$ can be deduced according to the grating equation, and then, according to the location shift equation, $\phi(x,y)$ becomes to two times its value when $m = 1$, which means the OAM state in the second-order diffraction will double its original OAM topological charge number in the first-order diffraction. Therefore, the high-order diffraction m will lead to high-order OAM states. It is the same principle of a fork-grating to generation OAM beams with a higher topological charge on its higher diffraction order. The evident intensity and phase distributions in Fig. 5 demonstrate the doubled OAM states brought by the second-order diffraction. Theoretically, if we can stretch the graphene OAM metalens larger, it is possible to obtain clear doughnut-shaped foci with the topological charge three times of the original OAM states. In this way, the topological charge of the OAM can be tuned using different diffraction orders, which can only be achieved uniquely by using the diffractive metalenses. Therefore, we numerically demonstrate in-situ tuning of topological charges through lateral stretching of ultrathin metalenses in simulation.

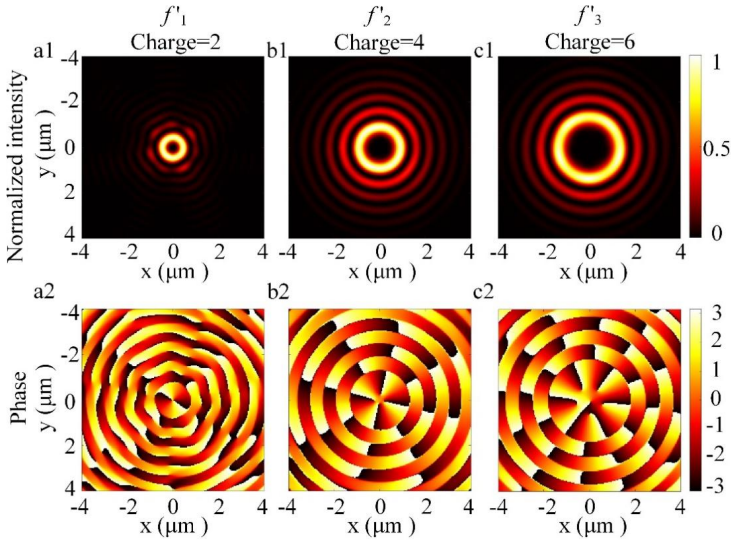

Fig. 5. Normalized intensity and phase distributions on the x-y planes of the newly generated doughnut-shaped foci f'_1 (a1 and a2), f'_2 (b1 and b2), and f'_3 (c1 and c2) when the SR is 2. The topological charges are 2, 4, and 6, respectively.

As the focusing efficiency (FE) is one of the most important parameters in generating high-order OAM states, we calculate the FE of all the doughnut-shaped foci. The relationship between each doughnut-shaped focal spot's FE with SR is plotted in Fig. 6. The FE here is defined as the doughnut intensity in the focal plane (4 μm × 4 μm) divided by the intensity immediately behind the corresponding annular part of the multifocal graphene OAM metalens. As the SR increases, the FEs of all the three doughnut-shaped foci f_1, f_2, and f_3 decrease; The FEs of the three new doughnut-shaped foci f'_1, f'_2, and f'_3 increase with the increase of SR. In general, considering

Optics EXPRESS

the diffraction efficiency follows the rule that the inner part of the metalens contributes more efficiently than the outer part to the focused beam. and as the outer areas increase faster than the inner areas, more absolute intensity comes in from the outer regions. There is a trade-off between FE and total intensity. As it is impossible that the FEs of high-order diffraction can continuously increase, there will be a critical value of SR for the highest FE of each diffraction order, which should be considered in the dynamic multifocal graphene OAM metalens design.

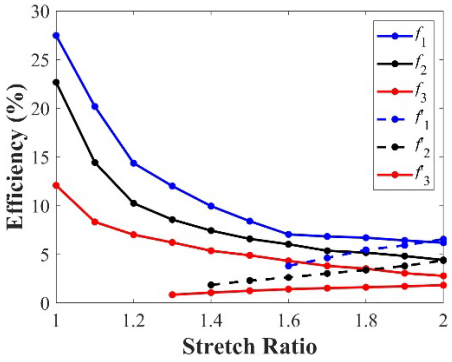

Fig. 6. Focusing efficiency of the three-focal graphene OAM metalens with stretch ratio.

3. Conclusion

In conclusion, a multifocal graphene OAM metalens has been designed by using spatially multiplexed single-focus graphene OAM metalenses with different focal lengths and topological charges based on the detour phase technique. The multifocal metalens can achieve doughnut-shaped foci with highly uniform intensity distributions at different focal lengths. The dynamic tuning of the focal lengths and the topological charges via lateral stretching was also studied theoretically. At small SR values, the focal length of each lens can be tuned without changing its topological charges. In addition, second-order foci with higher topological charges can also be generated when the SR is large. Therefore, by simulation, we numerically demonstrate a stretch-tunable multifocal graphene OAM metalens that can simultaneously vary its focal lengths and topological charges. This work opens up new possibilities for the design of OAM metalenses to meet different requirements. Furthermore, the ultrathin and flat features of the proposed graphene OAM metalens can be integrated readily into optical/photonic devices to generate and detect OAM beams simultaneously; this feature will find a broad range of applications. In addition, the new design method can be applied generally to the design of different OAM photonic devices with size miniaturization and integration capabilities.

Funding. National Natural Science Foundation of China (62175162, 62205214); Natural Science Foundation of Guangdong Province (2016A030310130); Foundation of Guangdong Education Committee (2020KTSCX117); China Postdoctoral Science Foundation (2021M692173); Science, Technology and Innovation Commission of Shenzhen Municipality (KQTD20170330110444030, KQTD20180412181324255); Science and Technology Foundation of Shenzhen City (20200814100534001).

Disclosures. The authors declare that there are no conflicts of interest related to this article.

Data availability. Data underlying the results presented in this paper may be obtained from the authors upon reasonable request.

References

1. L. Allen, M. W. Beijersbergen, R. Spreeuw, and J. Woerdman, "Orbital angular momentum of light and the transformation of Laguerre-Gaussian laser modes," Phys. Rev. A **45**(11), 8185–8189 (1992).
2. R. J. Voogd, M. Singh, and J. J. Braat, "The use of orbital angular momentum of light beams for optical data storage," Proc. SPIE **5380**, 387–392 (2004).

Optics EXPRESS

3. N. Bozinovic, Y. Yue, Y. Ren, M. Tur, P. Kristensen, H. Huang, A. E. Willner, and S. Ramachandran, "Terabit-scale orbital angular momentum mode division multiplexing in fibers," Science **340**(6140), 1545–1548 (2013).
4. A. Vaziri, G. Weihs, and A. Zeilinger, "Experimental two-photon, three-dimensional entanglement for quantum communication," Phys. Rev. Lett. **89**(24), 240401 (2002).
5. X. Zou and W. Mathis, "Scheme for optical implementation of orbital angular momentum beam splitter of a light beam and its application in quantum information processing," Phys. Rev. A **71**(4), 042324 (2005).
6. J. Oca and I. Masalo, "Flow pattern in aquaculture circular tanks: Influence of flow rate, water depth, and water inlet & outlet features," Aquac Eng. **52**, 65–72 (2013).
7. F. Tamburini, G. Anzolin, G. Umbriaco, A. Bianchini, and C. Barbieri, "Overcoming the Rayleigh criterion limit with optical vortices," Phys. Rev. Lett. **97**(16), 163903 (2006).
8. M. P. MacDonald, L. Paterson, K. Volke-Sepulveda, J. Arlt, W. Sibbett, and K. Dholakia, "Creation and manipulation of three-dimensional optically trapped structures," Science **296**(5570), 1101–1103 (2002).
9. M. Padgett and R. Bowman, "Tweezers with a twist," Nat. Photonics **5**(6), 343–348 (2011).
10. G. Molina-Terriza, J. P. Torres, and L. Torner, "Twisted photons," Nat. Phys. **3**(5), 305–310 (2007).
11. E. Karimi, B. Piccirillo, E. Nagali, L. Marrucci, and E. Santamato, "Efficient generation and sorting of orbital angular momentum eigenmodes of light by thermally tuned q-plates," Appl. Phys. Lett. **94**(23), 231124 (2009).
12. M. W. Beijersbergen, L. Allen, H. Van der Veen, and J. Woerdman, "Astigmatic laser mode converters and transfer of orbital angular momentum," Opt. Commun. **96**(1-3), 123–132 (1993).
13. M. Padgett and L. Allen, "Orbital angular momentum exchange in cylindrical-lens mode converters," J. Opt. B: Quantum Semiclassical Opt. **4**(2), S17–S19 (2002).
14. Y. Yan, J. Wang, L. Zhang, J.-Y. Yang, I. M. Fazal, N. Ahmed, B. Shamee, A. E. Willner, K. Birnbaum, and S. Dolinar, "Fiber coupler for generating orbital angular momentum modes," Opt. Lett. **36**(21), 4269–4271 (2011).
15. K. Sueda, G. Miyaji, N. Miyanaga, and M. Nakatsuka, "Laguerre-Gaussian beam generated with a multilevel spiral phase plate for high intensity laser pulses," Opt. Express **12**(15), 3548–3553 (2004).
16. V. V. Kotlyar, A. A. Almazov, S. N. Khonina, V. A. Soifer, H. Elfstrom, and J. Turunen, "Generation of phase singularity through diffracting a plane or Gaussian beam by a spiral phase plate," J. Opt. Soc. Am. A **22**(5), 849–861 (2005).
17. T. Lei, M. Zhang, Y. Li, P. Jia, G. N. Liu, X. Xu, Z. Li, C. Min, J. Lin, and C. Yu, "Massive individual orbital angular momentum channels for multiplexing enabled by Dammann gratings," Light: Sci. Appl. **4**(3), e257 (2015).
18. B. Wang, W. Liu, M. Zhao, J. Wang, Y. Zhang, A. Chen, F. Guan, X. Liu, L. Shi, and J. Zi, "Generating optical vortex beams by momentum-space polarization vortices centred at bound states in the continuum," Nat. Photonics **14**(10), 623–628 (2020).
19. E. Karimi, S. A. Schulz, I. De Leon, H. Qassim, J. Upham, and R. W. Boyd, "Generating optical orbital angular momentum at visible wavelengths using a plasmonic metasurface," Light: Sci. Appl. **3**(5), e167 (2014).
20. H. Chung, D. Kim, E. Choi, and J. Lee, "E-Band Metasurface-Based Orbital Angular Momentum Multiplexing and Demultiplexing," Laser Photonics Rev. **16**(16), 2100456 (2022).
21. Y. Yan, Y. Yue, H. Huang, Y. Ren, N. Ahmed, M. Tur, S. Dolinar, and A. Willner, "Multicasting in a spatial division multiplexing system based on optical orbital angular momentum," Opt. Lett. **38**(19), 3930–3933 (2013).
22. G. Gibson, J. Courtial, M. J. Padgett, M. Vasnetsov, V. Pas'ko, S. M. Barnett, and S. Franke-Arnold, "Free-space information transfer using light beams carrying orbital angular momentum," Opt. Express **12**(22), 5448–5456 (2004).
23. X. Bai, F. Kong, Y. Sun, G. Wang, J. Qian, X. Li, A. Cao, C. He, X. Liang, and R. Jin, "High-efficiency transmissive programmable metasurface for multimode OAM generation," Adv. Optical Mater. **8**(17), 2000570 (2020).
24. K. Guo, Q. Zheng, Z. Yin, and Z. Guo, "Generation of mode-reconfigurable and frequency-adjustable OAM beams using dynamic reflective metasurface," IEEE Access **8**, 75523–75529 (2020).
25. R. C. Devlin, A. Ambrosio, N. A. Rubin, J. B. Mueller, and F. Capasso, "Arbitrary spin-to–orbital angular momentum conversion of light," Science **358**(6365), 896–901 (2017).
26. Y. Wu, L. Kang, and D. H. Werner, "Active quasi-BIC optical vortex generators for ultrafast switching," New J. Phys. **24**(3), 033002 (2022).
27. S. Wei, G. Cao, H. Lin, X. Yuan, M. Somekh, and B. Jia, "A varifocal graphene metalens for broadband zoom imaging covering the entire visible region," ACS Nano **15**(3), 4769–4776 (2021).
28. X. Li, S. Wei, G. Cao, H. Lin, Y. Zhao, and B. Jia, "Graphene metalens for particle nanotracking," Photonics Res. **8**(8), 1316–1322 (2020).
29. G. Cao, H. Lin, S. Fraser, X. Zheng, B. Del Rosal, Z. Gan, S. Wei, X. Gan, and B. Jia, "Resilient graphene ultrathin flat lens in aerospace, chemical, and biological harsh environments," ACS Appl. Mater. Interfaces **11**(22), 20298–20303 (2019).
30. H. Lin, B. C. Sturmberg, K.-T. Lin, Y. Yang, X. Zheng, T. K. Chong, C. M. de Sterke, and B. Jia, "A 90-nm-thick graphene metamaterial for strong and extremely broadband absorption of unpolarized light," Nat. Photonics **13**(4), 270–276 (2019).
31. K.-T. Lin, H. Lin, T. Yang, and B. Jia, "Structured graphene metamaterial selective absorbers for high efficiency and omnidirectional solar thermal energy conversion," Nat. Commun. **11**(1), 1389 (2020).
32. X. H. Ren, X. Chen, J. Liu, Q. Li, C. Li, G. Xue, J. Jia, L. Cao, and A. Sahu, "Athermally photoreduced graphene oxides for three-dimensional holographic images," Nat. Commun. **6**(1), 6984 (2015).

Optics EXPRESS

33. X. Zheng, B. Jia, H. Lin, L. Qiu, D. Li, and M. Gu, "Highly efficient and ultra-broadband graphene oxide ultrathin lenses with three-dimensional subwavelength focusing," Nat. Commun. **6**(1), 8433 (2015).
34. S. Wei, G. Cao, H. Lin, H. Mu, W. Liu, X. Yuan, M. Somekh, and B. Jia, "High tolerance detour-phase graphene-oxide flat lens," Photonics Res. **9**(12), 2454–2463 (2021).
35. Y.-H. Yu, Z.-N. Tian, T. Jiang, L.-G. Niu, and B.-R. Gao, "Fabrication of large-scale multilevel phase-type Fresnel zone plate arrays by femtosecond laser direct writing," Opt. Commun. **362**, 69–72 (2016).
36. B. R. Brown and A. W. Lohmann, "Complex spatial filtering with binary masks," Appl. Opt. **5**(6), 967–969 (1966).
37. C. Min, J. Liu, T. Lei, G. Si, Z. Xie, J. Lin, L. Du, and X. Yuan, "Plasmonic nano-slits assisted polarization selective detour phase meta-hologram," Laser Photonics Rev. **10**(6), 978–985 (2016).
38. T.-C. Poon, *Digital holography and three-dimensional display: Principles and Applications* (Springer Science & Business Media, 2006).
39. V. Kotlyar, A. Kovalev, A. Porfirev, and E. Kozlova, "Orbital angular momentum of a laser beam behind an off-axis spiral phase plate," Opt. Lett. **44**(15), 3673–3676 (2019).
40. V. V. Kotlyar, A. A. Kovalev, and A. P. Porfirev, "Calculation of fractional orbital angular momentum of superpositions of optical vortices by intensity moments," Opt. Express **27**(8), 11236–11251 (2019).
41. G. Cao, X. Gan, H. Lin, and B. Jia, "An accurate design of graphene oxide ultrathin flat lens based on Rayleigh-Sommerfeld theory," Opto-Electron. Adv. **1**(7), 18001201 (2018).